Deciphering Tumour Tissue Organization by 3D Electron Microscopy and machine learning

Baudouin Denis de Senneville, Fatma Zohra Khoubai, Marc Bevilacqua, Alexandre Labedade, Kathleen Flosseau, Christophe Chardot, Sophie Branchereau, Jean Ripoche, Stefano Cairo, Etienne Gontier, et al.

communications biology

ARTICLE

https://doi.org/10.1038/s42003-021-02919-z OPEN

Deciphering tumour tissue organization by 3D electron microscopy and machine learning

Baudouin Denis de Senneville[1,2,11], Fatma Zohra Khoubai[3,11], Marc Bevilacqua[4], Alexandre Labedade[5], Kathleen Flosseau[6], Christophe Chardot[7], Sophie Branchereau[8], Jean Ripoche[9], Stefano Cairo[6,10,12], Etienne Gontier[4,12]✉ & Christophe F. Grosset[3,12]✉

Despite recent progress in the characterization of tumour components, the tri-dimensional (3D) organization of this pathological tissue and the parameters determining its internal architecture remain elusive. Here, we analysed the spatial organization of patient-derived xenograft tissues generated from hepatoblastoma, the most frequent childhood liver tumour, by serial block-face scanning electron microscopy using an integrated workflow combining 3D imaging, manual and machine learning-based semi-automatic segmentations, mathematics and infographics. By digitally reconstituting an entire hepatoblastoma sample with a blood capillary, a bile canaliculus-like structure, hundreds of tumour cells and their main organelles (e.g. cytoplasm, nucleus, mitochondria), we report unique 3D ultrastructural data about the organization of tumour tissue. We found that the size of hepatoblastoma cells correlates with the size of their nucleus, cytoplasm and mitochondrial mass. We also found anatomical connections between the blood capillary and the planar alignment and size of tumour cells in their 3D milieu. Finally, a set of tumour cells polarized in the direction of a hot spot corresponding to a bile canaliculus-like structure. In conclusion, this pilot study allowed the identification of bioarchitectural parameters that shape the internal and spatial organization of tumours, thus paving the way for future investigations in the emerging onconanotomy field.

[1] CNRS, University of Bordeaux, "Institut de Mathématiques de Bordeaux" (IMB), UMR5251, 351 cours Libération, F-33400 Talence, France. [2] INRIA Bordeaux, MONC team, 200 av Vieille Tour, F-33400 Talence, France. [3] Univ. Bordeaux, INSERM, Biotherapy of Genetic Diseases, Inflammatory Disorders and Cancer, BMGIC, U1035, MIRCADE team, 146 rue Léo Saignat, 33076 Bordeaux, France. [4] Univ. Bordeaux, CNRS, INSERM, Bordeaux Imaging Centre, BIC, UMS 3420, US 4, F-33000 Bordeaux, France. [5] Alexandre Labedade, freelance, F-33870 Vayres, France. [6] XenTech Company, Genopole Campus 3, 4 Rue Pierre Fontaine, F-91000 Évry-Courcouronnes, France. [7] Chirurgie Pédiatrique-Transplantation, Hôpital Necker-Enfants Malades, Assistance Publique Hôpitaux de Paris, 149 rue de Sèvres, F-75015 Paris, France. [8] Paediatric Surgery and Liver Transplant unit, Hôpital Bicêtre, Assistance Publique Hôpitaux de Paris – Université Paris Saclay, 78 rue du Général Leclerc, F-94270 Le Kremlin-Bicêtre, France. [9] Univ. Bordeaux, INSERM, retired, 146 rue Léo Saignat, 33076 Bordeaux, France. [10] Istituto di Ricerca Pediatrica, Corso Stati Uniti 4, 35127 Padova, Italy. [11] These authors contributed equally: Baudouin Denis de Senneville, Fatma Zohra Khoubai. [12] These authors jointly supervised this work: Stefano Cairo, Etienne Gontier, Christophe F. Grosset. ✉email: etienne.gontier@u-bordeaux.fr; christophe.grosset@inserm.fr

Diagnostic, prognostic and predictive clinical cancer studies are mainly based on the analysis of tissue sections in two dimensions (2D). However, tumours often present a complex architecture that 2D imaging cannot capture. Tumour cells establish composite interactions with the surrounding cancerous cells, extracellular matrix and stromal components, including blood capillaries and immune cells. In recent investigations, we noted that various hepatoma cells engrafted on the chick embryo chorioallantoic membrane (CAM) were arranged histologically and microscopically in a lineage-specific way while growing in a comparable controlled environment[1,2]. Moreover, pathological tumour atlases display a multitude of 2D images with tumour tissues whose cells are organized differently while belonging to the same category of cancer (http://www.pathologyatlas.ro; https://www.proteinatlas.org; https://atlases.muni.cz). These observations suggest that the structural organization of tumour tissue changes from one sample to another and is likely controlled by environmental and genetic factors such as the tissue origin, state of differentiation, genetic programme, the mutations they harbour, the activated molecular pathways, and the surrounding stromal components such as blood capillaries. Moreover, these interactions are dynamic and vary as the cancer progresses and metastasizes. To shed light on this critical issue, we investigated the ultrastructural pattern of cancer tissue.

The applications of 3D electron microscopy (EM) are still under development. Since its advent in the 1930s, EM has allowed the in-depth analysis of a wide range of biological samples. Transmission electron microscopy (TEM) and scanning electron microscopy (SEM) are routinely used to collect ultrastructural data from biological specimens at nanoscale resolution and to correlate structural images with biological functions. Although effective, these techniques produce images only in two dimensions. Therefore, investigating a large volume (100–1000 pL) of biological tissue in 3D at a high resolution was hardly possible until the development of 3D EM technologies including serial block-face (SBF)-SEM and Focused Ion Beam-SEM[3–6].

Hepatoblastoma (HB) is the most common form of liver cancer in young children. Recently, we reported the classification of these paediatric tumours in three groups, the use of Velcade® as a new therapeutic option for the treatment of aggressive HB and the development of an HB model in chick embryo for biological studies[1,7,8]. We also developed HB-patient-derived xenografts (PDX), a tumour model that recapitulates the histological, genetic and biological characteristics of parental HB[9]. Here, we used SBF-SEM to investigate the 3D internal organization of HB samples obtained from HB PDXs. Following image acquisition by SBF-SEM, we gathered quantitative data about the ultrastructure of tumour tissue using 3D imaging tools, mathematical algorithms and deep-learning approaches. We accurately measured the size of tumour cells and their main subcellular components (e.g. nucleus, mitochondria and cytoplasm), their planar alignment, their spatial orientation and the distance between the cells and a blood capillary. Results validate the relevance of our integrated workflow using wide-field 3D EM and computational approaches to investigate the deep internal architecture of HB tissue and the spatial organization of the tumour cells. These structural and functional data pave the way for future investigations in the emerging field of onconanotomy.

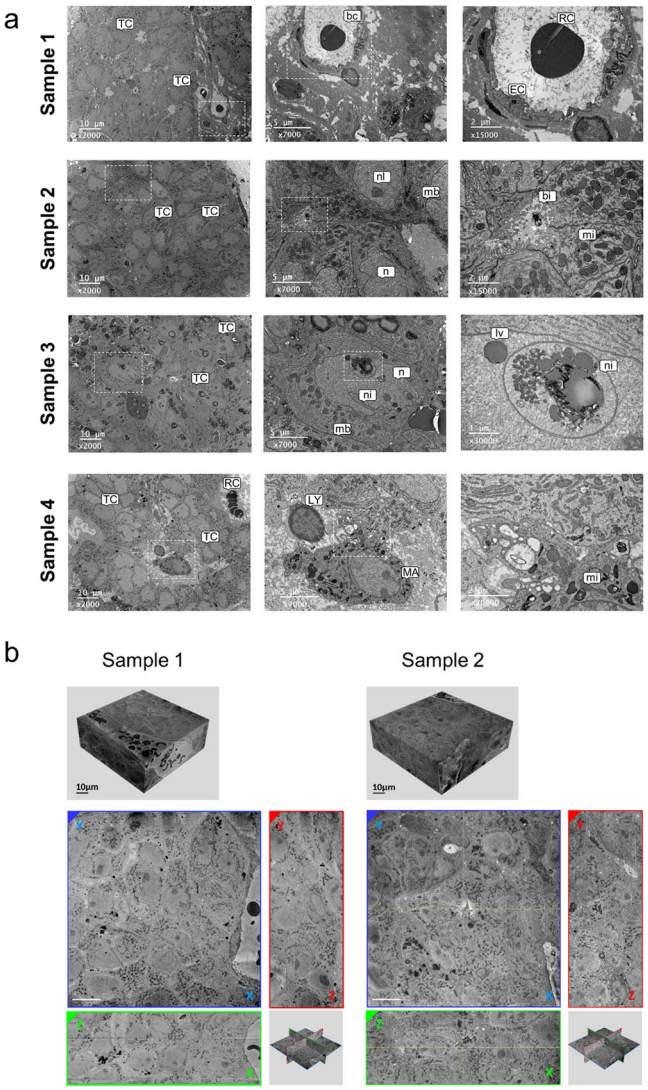

Fig. 1 Analysis of HB PDXs by EM. a Analysis of four HB PDX by TEM at different magnifications. White dotted-line frame: Region-of-interest corresponding to immediately higher magnification. bc, blood capillary; bi, bile canaliculus-like structure; EC, endothelial cells; MA, macrophage; lv, lipid vesicles; mb; plasma membrane; mi, mitochondrion; n, nucleus; ni, nuclear invagination; nl, nucleolus; LY, lymphocyte; RC, red cells; TC, tumour cell. **b** Top panels: SBF-SEM stacks from two samples. Bottom panels: Extracted images of orthogonal plane from different faces of reconstructed volume (*XY*, *YZ*, *XZ*), whose positions are displayed on orthoslice view positions inside stack. Scale bar = 10 µm.

Results

Image acquisition by EM and SBF-SEM of HB PDX tissues. To study the 3D organization of HB-PDX tissues, we adapted the protocol described by Deerinck et al.[10] to tumour samples (Supplementary Fig. 1) and analysed the ultrastructural morphology and the region of interest (ROI) of each stained sample by TEM using ultrathin sections. Figure 1a shows that the staining of the four samples was uniform and well contrasted and that all HB tissues retained their structure of origin. For example, membranes, mitochondria, endoplasmic reticulum, nuclei, lipid droplets and circulating red blood cells into capillaries ("bc") were clearly identifiable and typical with an excellent grey tone scale. The morphology of endothelial and immune cells was typical. Intercellular spaces were also visible and identified as bile canaliculus-like structures ("bi", sample 2)[11,12], which are indicative of liver-derived tissue. Overall, these results demonstrated the preservation of the ultrastructure of our HB samples following fixation and staining procedures.

Next, we analysed two HB PDXs by SBF-SEM and acquired high-resolution images in *X* and *Y* along the *Z*-axis to produce a substantial volumetric view of each sample. To obtain both image quality and detailed volumetric information, the acquired volume

was about 70 µm × 70 µm × 25 µm (pixel time = 10 µs, pixel size = 15 nm). After acquisition, the images were aligned to obtain 3D stacks (Fig. 1b; Sample 1: 250 images, 113.9 pL; Sample 2: 246 images, 121.6 pL). While volumetric image resolution was not isotropic (15 nm lateral resolution versus 100 nm depth resolution), ultrastructural features within the 3D stack were perfectly maintained and identifiable, allowing us to visualize the cells and their subcellular components within the tumour samples from any angle of view on the three axes (Fig. 1b).

3D organization of individual tissue components. Following stack reconstruction, we analysed the tissue features in tumour Sample 1 (Supplementary Fig. 2a, b, Supplementary Video 1). Using Ilastik[13] and VAST-Lite[14] software, we manually segmented a blood capillary and its circulating red and white blood cells (one leucocyte and one structure evoking a dendritic cell or a platelet cluster) (Supplementary Fig. 2c, f, Supplementary Video 1). The volume of the blood capillary portion irrigating the tissue was 11.3 pL and the 11 entirely segmented murine red blood cells were 61.92 ± 16.26 µm^3 in size (Supplementary Fig. 2c–f, Supplementary Data 1 and Supplementary Video 1). Next, we manually segmented a tumour cell from Sample 2 by delimitating the cytoplasm, the nucleus and the mitochondria. Again, the 3D digital representation allowed volumetric quantification of the cell and its cytoplasm, nucleus and mitochondrial network (970.6, 657.1, 313.6 and 64.6 µm^3, respectively), as well as affording a morphologic view of the tumour cell in its 3D environment (Supplementary Fig. 3; Supplementary Video 2). The size of this tumour cell was consistent with the size range of HB cells[15,16].

Reconstruction of tumour 3D organization by semi-automated segmentation. Although it produces accurate data, manual segmentation is too laborious and time-consuming to allow the analysis of hundreds of cells constituting a stack of about 110–120 pL. To overcome this problem and anticipate the analysis of larger volumes of tumour (>200 pL), we implemented a semi-automatic segmentation procedure comprising the manual segmentation of the cytoplasm and nucleus of cells on 1 out of 10 images in the stack form Sample 2 and an automatic segmentation algorithm of ROI by proximal propagation along the *Z* axis (Supplementary Fig. 4). This procedure allowed us to segment partially and entirely 182 tumour cells, 113 nuclei, 1 immune cell and 3 portions of the same blood capillary (Fig. 2a–c, Supplementary Fig. 5, Supplementary Video 3). The elongated shape of the immune cell, the presence of many vacuoles in its cytoplasm and its location near the blood capillary may suggest of a tumour-infiltrating macrophage (Supplementary Fig. 5, Supplementary Video 3). Following the alignment in a plane of 47 tumour cells with a complete nucleus, we found that 36 tumour cells (76.6%) and 35 nuclei (74.5%) had an inclination angle of 0 to 20° (relative to the best alignment plane, see Online Methods), while the inclination angle of the blood capillary was 8° (Fig. 2d, e, Supplementary Fig. 6, Supplementary Data 1, Supplementary Video 4). These data suggested that the blood capillary may influence the spatial arrangement of tumour cells.

Next, we measured the tumour cell polarity (in the sense of attraction toward a particular object) using a vectoral approach (see Online Methods). In both cases, data showed that a set of tumour cells polarized in the direction of a hot spot corresponding to a bile canaliculus-like structure (Fig. 3, Supplementary Fig. 7, Supplementary Video 5)[11,12]. Numerous membrane protrusions were visible at the boundary between the bile canaliculus-like structure and the canalicular membrane of the surrounding tumour cells (Supplementary Fig. 7, Supplementary Video 5). This structure into which hepatocytes excrete their metabolic agents after enzymatic neutralization is specific to normal liver tissue[15] and has been reported to be remnant in some HB[11,12].

Finally, we focused our attention on the 21 fully segmented tumour cells contained in sample 2. Mitochondria are key organelles of tumour cell function but too numerous (between 200 and 400 per cell) and small in size to be manually segmented from our whole tissue sample. Thus, a deep-learning algorithm was fed using data from mitochondria manually segmented on one single cell. Next, we performed two successive cycles of automatic segmentation by deep-learning propagation combined with manual segmentation clean-up of segmented mitochondria (see Methods). Following this segmentation procedure, the size of these cells and their cytoplasm, nucleus and mitochondrial network was measured and component/cell ratios were calculated (Supplementary Fig. 8a, b, Supplementary Data 1). In line with the known relationship between the size or number of organelles and the size of the cell[17,18], we found that the larger the tumour cell, the larger its cytoplasm, global mitochondrial network and nucleus (Fig. 4a, Supplementary Data 1). By measuring the distance between each of these cellular components and the blood capillary, we also found that the tumour cells located near the blood capillary were significantly larger than those located away from it (Fig. 4b, c, Supplementary Data 1, Supplementary Video 6). This inverse correlation with the distance to the capillary was also observed when considering the cytoplasm and the mitochondrial network (the latter having the highest correlative value) but not the nuclei (Fig. 4c, Supplementary Fig. 9a–c, Supplementary Data 1, Supplementary Video 6). Altogether, these data suggested that the size of HB cells and their mitochondrial content is linked to the distance with blood capillary. These observations are in agreement with the decrease in mitochondrial mass in cells exposed to low oxygen supply[19,20].

Discussion

A still unanswered question is whether cells are distributed randomly in cancer tissue or if and how their organization is governed by physical and molecular factors reminiscent of the structure of normal tissue. In this pilot study, we used a 3D EM approach named onconanotomy, i.e. a workflow to analyse in depth the architecture of tumour samples using a combination of sample preparation, SBF-SEM imaging, computational approaches and infographic tools (see Technical workflow in Fig. 5). To the best of our knowledge, this is the first report investigating the complete ultrastructure of human tumour xenograft tissue by high-resolution 3D EM.

While automated segmentation with machine learning methods has become an essential technique for analysing the ultrastructure of all tissue and cell types, the main difficulty in our work laid in the construction of the learning database. At the very beginning of our study, we did not have any organelle segmentation available and we used manual segmentation. Thus, we developed semi-automatic approaches to accelerate the process. One can anticipate that a fully automated segmentation of major organelles (cytoplasm, nuclei, mitochondria, etc.), cell types (blood cells, immune cells, hepatocytes and tumour cells) and tissue structures (capillary, bile-canaliculus, etc.) is feasible (see Segmented tissue elements in Fig. 5) based on sufficiently populated training databases and given high potential of novel technologies in artificial intelligence.

Previous detailed reports on the 3D bioarchitectural organization of tumour are lacking to fully establish if our data are reflecting the real situation found in this pathological tissue. However, we found red and white cells circulating in a blood

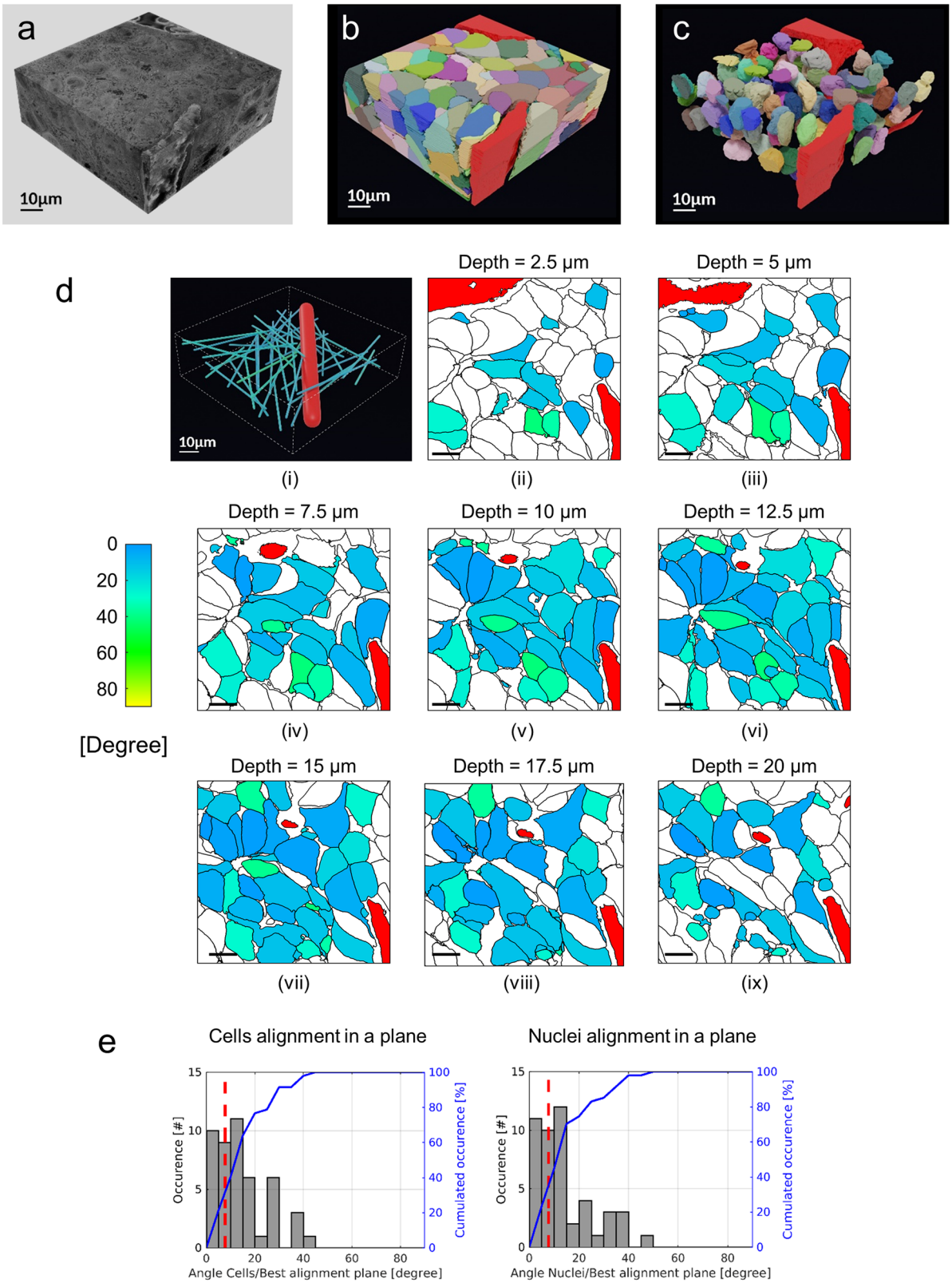

Fig. 2 Alignment of HB cells and nuclei. a Sample 2 stack. **b**, **c** Digital representation of (**a**) with 182 cells (**b**) and 113 nuclei (**c**). **d** Alignment of cells and blood capillary in a plane: (i) coloured sticks = main axis of tumour cells; red stick = main axis of blood capillary. (ii–ix) Angles between each main cell axis and the best alignment plane. 2D cross-sectional maps for increasing depth along *Z*-axis. Scale bar = 10 µm. **b**–**d** Blood capillary portions are in red. **e** Histograms of cells (left panel) and nuclei (right panel) alignment angles. Red dashed line: alignment angle of blood capillary.

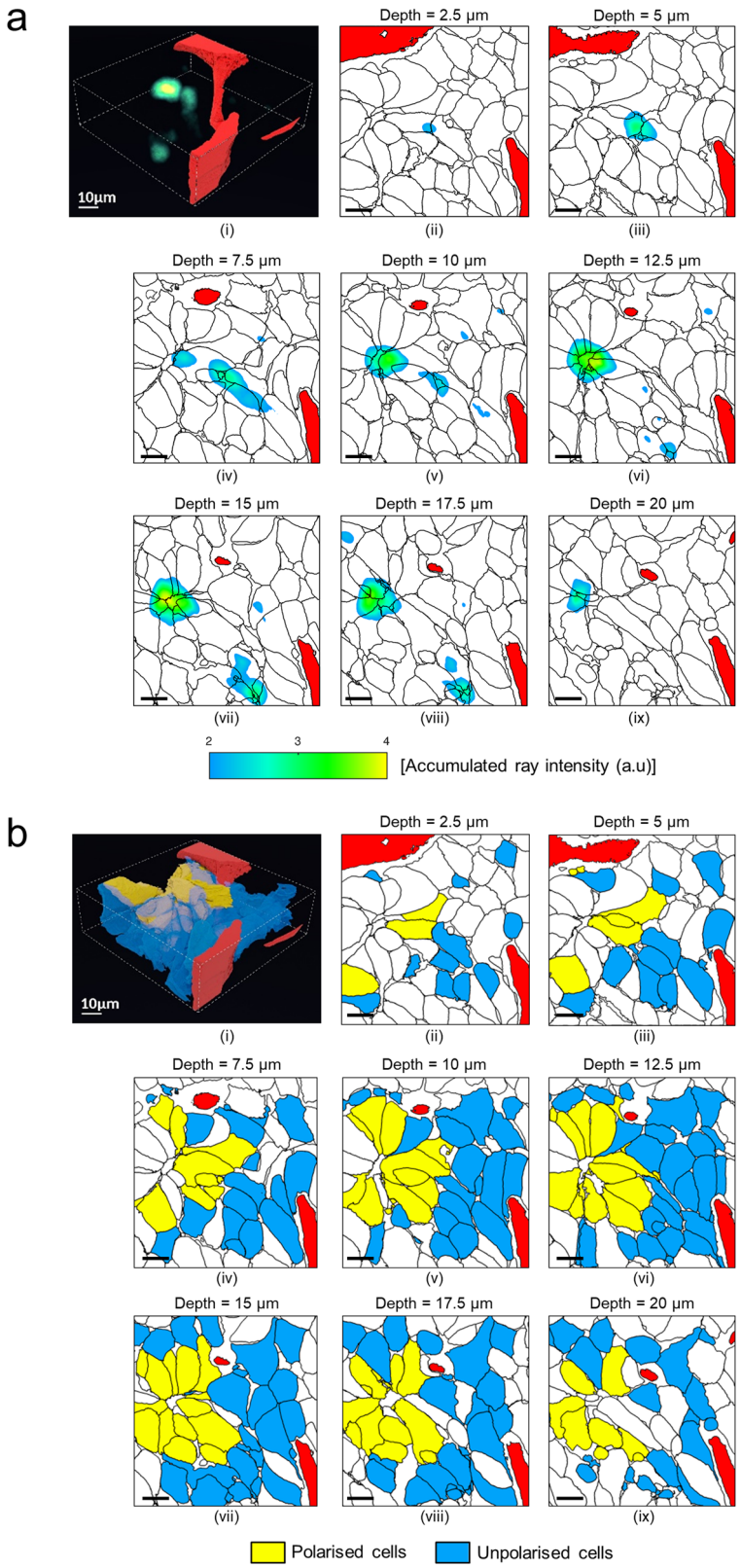

Fig. 3 Tumour cell cluster with polarized shape orientation. Only tumour cells with a complete nucleus are considered here. Blood capillary portions are in red. **a** Accumulation map of virtual rays [Accumulated ray intensity [a.u]; voxel-by-voxel basis; see yellowish voxels] emitted by each cell along its main axis. (i) Reconstructed 3D image of accumulation map of virtual rays. (ii–ix) 2D cross-sectional maps for increasing depth along the *Z*-axis. **b** Binary classification of polarised/unpolarised cells: (i) Reconstructed 3D image of polarised/unpolarised cells. 17 cells (in yellow) emitted virtual rays reaching the main accumulation region observable in panel (vii) (accumulated ray intensity >3.5). a.u., arbitrary unit. (ii–ix) 2D cross-sectional maps for increasing depth along the *Z*-axis. Scale bar = 10 µm.

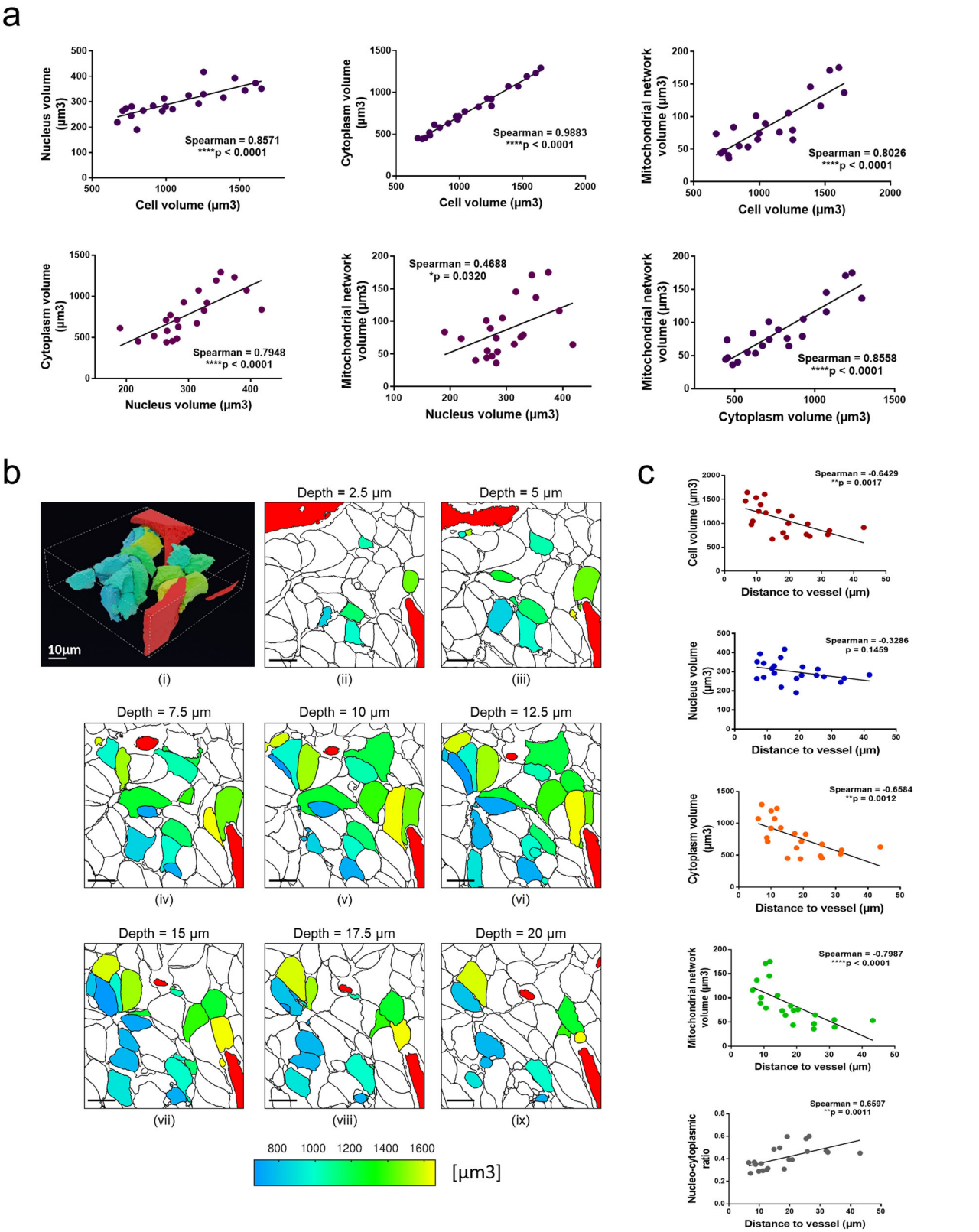

Fig. 4 3D organization of typical cellular and subcellular structures. Only 21 entirely contained cells are considered here. **a** Volumetric correlations between cytoplasm, nucleus and mitochondrial network. **b** Cell sizes related to distance from blood capillary: (i) Reconstructed 3D image of cells and blood capillary. Cell colour is related to its volumetric size. (ii–ix) 2D cross-sectional maps for increasing depth along the Z-axis. (i–ix) Blood capillary portions are in red. Scale bar = 10 µm. **c** Correlation between distance to blood capillary and cellular/subcellular structures or nucleocytoplasmic ratio. **a**, **c** Spearman correlations. *r* and *p* values are as indicated in corresponding graph.

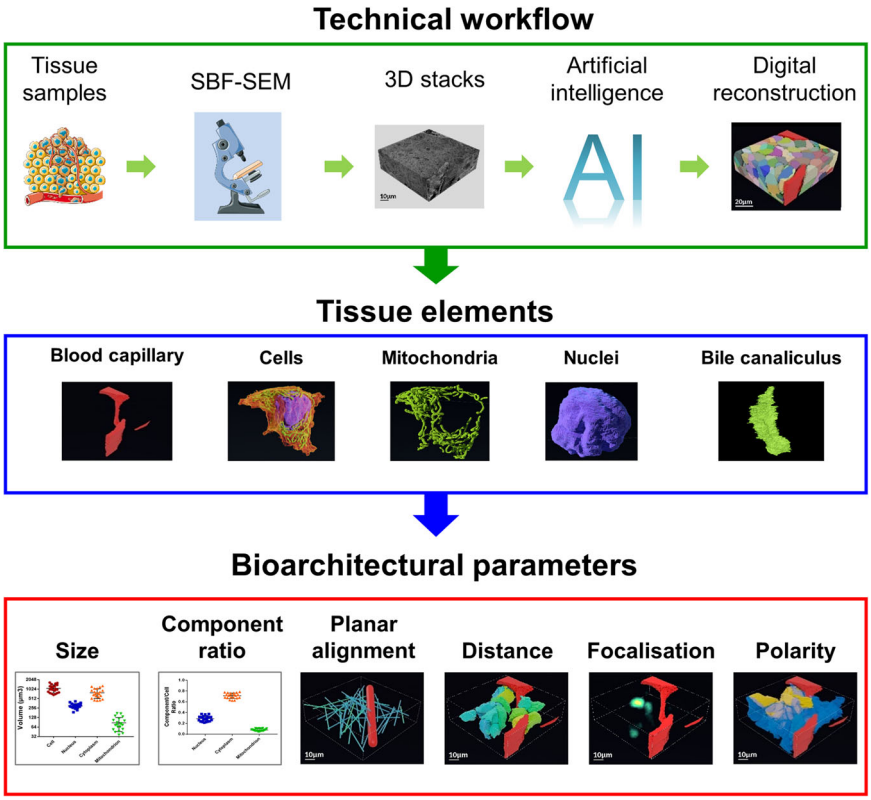

Fig. 5 Graphical summary of the 3D EM approach used to study tumour tissue architecture. The figure is divided into three steps: the technical workflow, the segmented tissue elements and the different bioarchitectural parameters used to analyse the 3D organization of tumour tissue.

capillary portion (Supplementary Fig. 2, Supplementary Video 1), a direct correlation between the size of tumour cells, of mitochondria and of nuclei (Fig. 4a) and tumour cells polarizing in the direction of a hot spot corresponding to a bile canaliculus-like structure (Fig. 3, Supplementary Video 5). Together, these data suggest that our samples preparation fully preserved the HB sample ultrastructure following fixation and staining procedures, and consequently, that our structural observations are reliable. Our data also demonstrate the feasibility of our methodology to study the 3D organization of tumoral tissue using specific bioarchitectural parameters (Fig. 5) and the potential advance it represents in understanding cancer biology. The information obtained on the organization of liver cancer cells throws light on tumour physiology. In particular, it suggests that blood capillaries could determine the ultrastructure of tumoral tissue by controlling the alignment and size of tumour cells and their subcellular components. However, further studies are required to strengthen this hypothesis. In addition, we found that a bile canaliculus-like structure guides the spatial arrangement and the polarity of tumour cells in HB tissue, as it does in normal liver tissue to subsume the physiological functions of normal hepatocytes[15].

This study is a preliminary attempt to unravel the internal architecture of tumoral tissue and has limitations. First, it is difficult to automatically segment-specific structures such as tumour-infiltrating macrophages and endoplasmic reticulum. The procedure requires visual control and manual correction, which are time-consuming. Second, our sample set was small. Future studies with a larger number and variety of tumoral tissues would allow us to generate more digitalized samples that in turn would improve the automatic segmentation process. A larger dataset would also allow us to better evaluate whether blood capillaries and bile canaliculus-like structures, which are common features in HB and more generally in epithelial liver tumours, influence the polarity and spatial organization of tumour cells and their organelles. These techniques coupled with current omic approaches would provide much insight into the relationship between the structural organization of tumours, and their cellular functions and metabolic activities.

Future possible directions of onconanotomy-based exploratory studies are the following: (a) analysing virtually all types of solid tumours to generate a virtual 3D biorepository whose data would be particularly valuable in the case of rare tumours or precious samples such as biopsies; (b) comparing matched tumour samples such as changes occurring before and after treatment or primary versus metastatic features, and (c) identifying structural subtypes and verifying their overlap with different histological groups such as embryonal versus foetal *versus* small undifferentiated cell subtypes described in HB[8,16]. Since this methodology is adapted to lab tumour models like cell xenografts, tumour-like spheroids and organoids, our combined approach could help investigators to clarify the role of genes and molecular pathways involved in the architecture of tumoral tissue and to investigate the response of tumour cells to drugs (e.g. checkpoint inhibitors, monoclonal antibodies) and treatments (e.g. radiotherapy). Finally, our approach is perfectly transferable to other biological kingdoms and fields based on tissue development including for instance plants, fungi, neuroscience, embryogenesis and biomaterials.

Based on our approach (Fig. 5), 3D EM users could measure valuable structural parameters (e.g. size, component ratio, polarity, etc.) and potential additional ones (e.g. cellular density, surface, texture, etc.) related to tumour tissue components using biopsies, tumour resections or lab models[4]. These analyses should help investigators (1) to better understand how a tumour tissue is spatially constructed, (2) to determine in a dynamic or comparative manner (e.g. at different tumour development periods) the close relationships between tumour cells and other tissue

elements (e.g. blood capillary, nerve endings, immune cells, etc.) and (3) to study in 3D the elements constituting a "tumour niche"[21]. Such investigations could also help to clarify the mechanisms by which the tissue is expanding while growing and in which direction, how tumour cells invade the surrounding tissue by outcompeting with non-tumoral cells and how the metastatic cells traverse the vascular wall. By performing comparative analysis, investigators could evaluate at a nanoscale level the efficacy of an antitumoral drug transported by the blood circulation on tumour cells. The implementation of our approach to histopathology practice may also provide additional biomarkers for the diagnosis, the prognosis, the drug-response prediction and help to stratify tumours. To sum up, our procedure should boost the interest of the scientific and clinical communities working in cancer for 3D EM technologies[4].

In conclusion, our study aims to foster the development of what we have termed onconanotomy, a novel research field in oncology, that will complement other innovative imaging technologies such as two-photon excitation microscopy (also known as 2PEF) and correlative light-electron microscopy (also known as CLEM). This field could be backed up by the development of open-source databanks gathering all 3D imaging data at a worldwide level in order to boost research and promote cooperation in cancer, as was previously the case with Gene databanks and Cell and Tissue atlases. By accessing 3D image databanks, investigators could upload valuable information and perform comparative investigations to unravel the ultrastructure of solid tumours. The potential focuses include cell-cell and cell-extracellular matrix interactions, intratumoral heterogeneity, pro-metastatic mechanisms, angiogenesis, drug response, therapeutic efficacy and regulatory factor gradation. We believe that, in few decades from now and thanks to digital approaches and artificial intelligence, these approaches could enrich the field of oncology with the support of other technologies such as single-cell RNA-seq, microfluidics and complex 3D lab models. It might especially provide ground-breaking insights into how cells disseminate and how drugs reach the targets cells. A better comprehension of the organization of tumour cells and clinical outcome could help in identifying the key structural parameters of cancers. In turn, this could lead to substantial advances in both the understanding of cancers and the treatments of adult and paediatric cancer patients.

Methods

Ethical clearance. PDX development program was approved by the Hospital ethics committee, each sample was implanted upon signature of the related informed consent form. Mice were maintained in specific pathogen-free animal housing at the Center for Exploration and Experimental Functional Research (CERFE, Evry, France) animal facility. All experimental procedures related to PDX development were conducted in accordance with French regulatory legislation concerning the protection of animals used for scientific purposes were approved by the CERFE animal facility ethics committee and by the Ministère de l'Agriculture et de l'Alimentation, France.

PDX establishment. At surgery, tumour fragments were sampled from the resected tumour and placed in cell culture medium supplemented with penicillin/streptomycin and with or without 5% BSA on ice. Tumour samples were chopped into 4 × 3 mm fragments and grafted in the interscapular region of 6-8 week-old female athymic nude mice (Athymic Nude-Foxn1nu, ENVIGO-Harlan Laboratories, Gannat, France). Tumour growth from the first implantation occurred with a delay spanning between 1 and 5 months. Growing tumours were serially transplanted onto recipient mice and underwent comparative examination to confirm preservation of their histological features. To immortalize each PDX, vials of 4 × 3 mm fragments from tumours at different passages were placed in a solution of 90% FCS/10% DMSO or glycerol, and stored at −150 °C.

PDX samples. PDX was generated in compliance with the informed consent form signed by the patients and developed as previously described[9]. The main clinical and genetic characteristics of HB PDX samples are shown in Supplementary Table 1.

PDX fragments fixation. For each model, 5 fragments (2 × 1 mm) were taken and placed in ice-cold fixing solution (2% PFA and 2.5% glutaraldehyde in 0.15 M Cacodylate + 2 mM $CaCl_2$ buffer). After 3-h fixation with gentle stirring, the fragments were transferred to a tube containing Cacodylate buffer and kept overnight at 4 °C before shipment to the Imaging platform.

Serial block-face scanning electron microscopy sample preparation. Tissue was prepared for SBF-SEM as previously described[10]. The samples were fixed with a 2% paraformaldehyde and 2,5% solution of glutaraldehyde in 0.15 M cacodylate buffer (pH 7.4) for 2 h at room temperature and then were washed 5 × 3 min in cold 0.15 M cacodylate buffer. En bloc contrast staining was performed by consecutive incubations in heavy metal containing solutions. The first staining step was a 1 h incubation on ice in 2% OsO_4 containing 1.5% potassium ferrocyanide in 0.15 M cacodylate buffer. After washing 5 × 3 min in ultrapure water, the samples were incubated for 20 min in a fresh thiocarbohydrazide solution (1% w/v in water) at room temperature. The next wash step was followed by incubation in 2% osmium in water at RT for 30 min and after washing 5 × 3 min in ultrapure water 2% uranyl acetate at 4 °C overnight. The following day, Walton's lead aspartate staining was performed for 30 min at 60 °C. For this, a 30 mM L-aspartic acid solution was used to freshly dissolve lead nitrate (20 mM, pH 5.5), the solution was filtered and blocks incubated for 30 min at 60 °C. After final washing steps, the samples were dehydrated using ice-cold solutions of 30%, 50%, 70%, 90%, 2×100% ethanol (anhydrous), 2 × 100% aceton, 10 min each. Resin embedding was done using Epon by first placing the samples in 25% aceton/Epon for 2 h, 50% aceton/Epon for 2 h, 75% aceton/epon for 2 h and followed by 2 incubations in 100% epon (overnight, 8 h). The samples were put in fresh epon's resin and placed at 60 °C for 48 h. Once the resin block were hardened, they were roughly cut with a razor blade to generate a pyramid shape and mounted on aluminium specimen pins using a silver filled conductive resin (Epotek-Delta microscopies, Mauressac, France). After 24 h of polymerisation at 60 °C, the samples were trimmed with a diamond knife (Diatome, Nidau, Switzerland). Silver filled conductive resin was used to electrically connect the edges of the tissue to the aluminium pin. The entire sample was then sputter coated with a 5–10 nm layer of gold to enhance conductivity.

Transmission electron microscopy. The samples were first analysed by TEM to control morphology and define the region of interest. Ultra-thin sections were cut and deposited on copper grids and observed with a Hitachi H7650 transmission electron microscope (Japan).

Serial block-face scanning electron microscopy imaging. The sample on the pin was placed into the carrier that fits into the3View ultramicrotome (3viewXP2-Gatan Inc., Pleasanton, CA, USA) on a ZEISS Gemini field emission gun SEM300 (Zeiss - Marly-le-Roi - France). The block face was imaged with an accelerating voltage at 1.2 kV using the Back scattered electron with a specific BSE Detector (On point - Gatan Inc., Pleasanton, CA, USA).

Pre-processing and structure segmentation. Image analysis was performed using three complementary software packages. Digital Micrograph (Gatan Inc., Pleasanton, CA, USA) was used to align the images with the Image Alignment plugin using the combined default filter (which combines soft rectangle and bandpass filters). The aligned images were saved in Gatan format "dm4" as a single stack. Fiji software was used to convert the 32-Bit images into 8-Bit images to be less resource-consuming and facilitate segmentation. Then the image was cropped to the optimal (larger) rectangular field of view, and the brightness and contrast were automatically adjusted (Z-scoring on a slice-by-slice basis). Finally, VAST-Lite software was used for the manual segmentation of the elements of interest (cells, nuclei and mitochondria)[14]. Image processing was done following the pipeline shown in Supplementary Fig. 10. All manual segmentation was done using an interactive drawing tablet and pen (Cintiq pro 5, Wacom).

The manual segmentation of both cells and nuclei was done only on 10% of the stack of images (1 image out of 10) using the VAST-Lite software[14]. These manual segmentations were propagated to neighbouring slices using a so-called « Optical Flow » algorithm (see "Source codes" section below) applied on the EM images, similar to the approach described by Huang T.C. et al.[22]. This procedure allowed us to segment partially and entirely 182 tumour cells, 113 nuclei in a relatively decent time frame (several weeks were mandatory). However, the segmentation of mitochondria turned out to be a different challenge. The reason is two-fold: (1) the volume of mitochondria is far lower the size of cells nuclei, preventing the use of the above-mentioned propagation strategy; (2) the number of mitochondria is much greater than the number of cells and nuclei, further hampering in turn the amount of work. Mitochondria were thus segmented manually on one single cell to feed a deep-learning algorithm (using a 3D U-net architecture[23] and an implementation based on Tensorflow 1.4 and Keras 2.2.4), which could be subsequently used for semi-automatic segmentation. The 3D U-Net architecture used for the segmentation of mitochondria is presented in Supplementary Fig. 11. The architecture is similar to the one proposed by Huo et al.[24]. We used one single input channel (i.e., the SBF-image). The loss function was a combination of categorical cross-entropy and Dice[25]. The optimizer algorithm was Adam with default parameters[26]. 100 epochs were performed and the batch size was equal to 1.

Due to limited GPU memory, we used a patch-wise strategy[27]: practically, local patches of 128 × 128 × 128 voxels were extracted in the training SBF image and used as inputs for the CNN. To finish, erroneous automatic segmentations of mitochondria were corrected manually using the VAST-Lite[14] and Ilastik[13] software.

Analysis of orientation of structures. Each cell, nucleus and capillary portion was characterized using its main axis. To this end, a Principal Component Analysis (PCA) was applied on the voxel coordinates within the segmented mask of a structure of interest. Only tumour cells with a complete nucleus were considered. The following two analyses were conducted.

Analysis of alignment in 2D plane of cells and nuclei. The main axes of cells were used to calculate the best 2D "alignment plane" (in the least-squares sense: we minimized the sum of squared differences between the observed main axes of cells, and the fitted value provided by a 2D plane equation). Angles between the main axis of each cell and the alignment plane were calculated. The same analysis was conducted subsequently for nuclei.

Determination of cell clusters with polarized shape orientation. 3D virtual rays were emitted by each cell along its main axis in both directions (the ray radius was a user-defined input parameter for the algorithm and was set to 15 µm, ray intensity proportional to the Euclidean distance to the main axis, with a value of 1 on the main axis). To this end, Bresenham's line algorithm[28] was employed and adapted to our needs. The accumulated beam intensity was calculated on a voxel-by-voxel basis. Cells emitting virtual rays reaching a specific accumulation region were subsequently selected. Thus, cells converging toward a common region could be listed.

Source codes. The code designed to identify the analyzed bioarchitectural parameters (alignment, volume, shape orientation) can be found in https://github.com/bsenneville/Onconanotomy/. The code implementing the above-mentioned optical flow algorithm employed for the semi-automatic segmentation of cells and nuclei can be found in https://github.com/bsenneville/2D_Optical_Flow/[29]. Both codes were developed under the commercial software Matlab ©1994-2021 The MathWorks, Inc.

Infographics. Blender version 2.90.1 (https://www.blender.org) was used to create the illustrations (images and Supplementary videos). The Cycles render engine was used for all the final renderings. To render polygonal meshes, the data were imported from VTK files using the BVTK addon (https://github.com/tkeskita/BVtkNodes). Depending on the data complexity, the meshes were decimated to lower the polygon count, but still preserving the overall shape and most of the details. For volumetric rendering, the original stack data was converted from a multi-page Tiff image file to a downscaled 2D tile map, which was then loaded and translated to a 3D volume into Blender using a custom shader setup. ImageJ (https://imagej.nih.gov/ij/), XNview (https://www.xnview.com) and the "montage" command line tool of ImageMagick (https://imagemagick.org/script/montage.php) were used for image conversion, downscaling and stitching. Downscaling is mandatory, since the original amount of data is not always practical to work with and is not necessary for the purpose of visualization.

Statistical analyses. Statistical analyses were performed using GraphPad Prism 7.05 software. Spearman's nonparametric correlation was used to compare the size of different cell components or the size of a specific component to the distance to a blood capillary. Results were considered significant when $p < 0.05$.

Reporting summary. Further information on research design is available in the Nature Research Reporting Summary linked to this article.

Data availability

The data that support the findings of this study are available within the paper and its Supplementary information files.

Received: 17 August 2021; Accepted: 12 November 2021;
Published online: 13 December 2021

References

1. Indersie, E. et al. MicroRNA therapy inhibits hepatoblastoma growth in vivo by targeting beta-catenin and Wnt signaling. *Hepatol. Commun.* **1**, 168–183 (2017).
2. Cartier, F. et al. New tumor suppressor microRNAs target glypican-3 in human liver cancer. *Oncotarget* **8**, 41211–41226 (2017).
3. Denk, W. & Horstmann, H. Serial block-face scanning electron microscopy to reconstruct three-dimensional tissue nanostructure. *PLoS Biol.* **2**, e329 (2004).
4. Riesterer, J. L. et al. A workflow for visualizing human cancer biopsies using large-format electron microscopy. *Methods Cell Biol.* **158**, 163–181 (2020).
5. Knott, G., Marchman, H., Wall, D. & Lich, B. Serial section scanning electron microscopy of adult brain tissue using focused ion beam milling. *J. Neurosci.* **28**, 2959–2964 (2008).
6. Titze, B. & Genoud, C. Volume scanning electron microscopy for imaging biological ultrastructure. *Biol. Cell* **108**, 307–323 (2016).
7. Indersie, E. et al. Tracking cellular and molecular changes in a species-specific manner during experimental tumor progression in vivo. *Oncotarget* **9**, 16149–16162 (2018).
8. Hooks, K. B. et al. New insights into diagnosis and therapeutic options for proliferative hepatoblastoma. *Hepatology* **68**, 89–102 (2018).
9. Nicolle, D. et al. Patient-derived mouse xenografts from pediatric liver cancer predict tumor recurrence and advise clinical management. *Hepatology* **64**, 1121–1135 (2016).
10. Deerinck, T. J., Bushong, E., Thor, A. & Ellisman, M. H. NCMIR methods for 3D EM: a new protocol for preparation of biological specimens for serial blockface scanning electron microscopy. *Microscopy* **1**, 6–8 (2010).
11. Dekmezian, R., Sneige, N., Popok, S. & Ordonez, N. G. Fine-needle aspiration cytology of pediatric patients with primary hepatic tumors: a comparative study of two hepatoblastomas and a liver-cell carcinoma. *Diagn. Cytopathol.* **4**, 162–168 (1988).
12. Pietsch, T. et al. Characterization of the continuous cell line HepT1 derived from a human hepatoblastoma. *Lab Invest* **74**, 809–818 (1996).
13. Berg, S. et al. ilastik: interactive machine learning for (bio)image analysis. *Nat. Methods* **16**, 1226–1232 (2019).
14. Berger, D. R., Seung, H. S. & Lichtman, J. W. VAST (volume annotation and segmentation tool): efficient manual and semi-automatic labeling of large 3d image stacks. *Front Neural Circuits* **12**, 88 (2018).
15. Cullen, J. M. & Stalker, M. J. in *Jubb, Kennedy & Palmer's Pathology of Domestic Animals* Vol. 2 (ed Grant Maxie, M.) 258–352.e251 (2016).
16. Lopez-Terrada, D. et al. Towards an international pediatric liver tumor consensus classification: proceedings of the Los Angeles COG liver tumors symposium. *Mod. Pathol.* **27**, 472–491 (2014).
17. Chan, Y. H. & Marshall, W. F. Scaling properties of cell and organelle size. *Organogenesis* **6**, 88–96 (2010).
18. Schmoller, K. M. The phenomenology of cell size control. *Curr. Opin. Cell Biol.* **49**, 53–58 (2017).
19. Fuhrmann, D. C., Wittig, I., Heide, H., Dehne, N. & Brune, B. Chronic hypoxia alters mitochondrial composition in human macrophages. *Biochim. Biophys. Acta* **1834**, 2750–2760 (2013).
20. Lages, Y. M. et al. Low oxygen alters mitochondrial function and response to oxidative stress in human neural progenitor cells. *PeerJ* **3**, e1486 (2015).
21. Laplane, L., Duluc, D., Larmonier, N., Pradeu, T. & Bikfalvi, A. The multiple layers of the tumor environment. *Trends Cancer* **4**, 802–809 (2018).
22. Huang, T. C. et al. Semi-automated CT segmentation using optic flow and Fourier interpolation techniques. *Comput Methods Prog. Biomed.* **84**, 124–134 (2006).
23. Ronneberger, O., Fischer, P. & Brox, T. U-net: Convolutional Networks for Biomedical Image Segmentation. In *International Conference on Medical Image Computing and Computer-Assisted Intervention* 234–241 (Springer, Cham, 2015) https://doi.org/10.1007/978-3-319-24574-4_28.
24. Huo, Y. et al. 3D whole brain segmentation using spatially localized atlas network tiles. *Neuroimage* **194**, 105–119 (2019).
25. Sugino, T. et al. Loss weightings for improving imbalanced brain structure segmentation using fully convolutional networks. *Healthcare (Basel)* **9**, https://doi.org/10.3390/healthcare9080938 (2021).
26. Kingma, D. P. & Ba, J. Adam: A Method for Stochastic Optimization. *CoRR* abs/1412.6980 (2015).
27. Liu, Y., Ren, Q. R., Geng, J. H., Ding, M. & Li, J. Y. Efficient patch-wise semantic segmentation for large-scale remote sensing images. *Sensors-Basel* **18**, 3232 (2018).
28. Bresenham, J. Algorithm for computer control of a digital plotter. *IBM Syst. J.* **4**, 25–30 (1965).
29. Zachiu, C., Papadakis, N., Ries, M., Moonen, C. & Denis de Senneville, B. An improved optical flow tracking technique for real-time MR-guided beam therapies in moving organs. *Phys. Med Biol.* **60**, 9003–9029 (2015).

Acknowledgements

This work was supported by the charity Eva pour la Vie, La Fondation ARC pour la Recherche sur le Cancer (contract N° PJA 20191209631), La Région Nouvelle-Aquitaine, La Fondation Groupama pour la Santé and Groupama Centre-Atlantique. Microscopy Imaging was performed at the Bordeaux Imaging Centre, which is a member of the FranceBioImaging national infrastructure (ANR-10-INBS-04). Computational analysis was carried out using the PlaFRIM experimental testbed, supported by Inria, CNRS (LABRI and IMB), Université de Bordeaux, Bordeaux INP and Conseil Régional

d'Aquitaine (see https://www.plafrim.fr/). Computer time for this study was provided by the computing facilities at MCIA (Mésocentre de Calcul Intensif Aquitain) of the Université de Bordeaux and of the Université de Pau et des Pays de l'Adour.

Author contributions

Fresh paediatric tumour fragments were provided by S.B. and C.C. HB-PBX were developed by XenTech company and provided by K.F. and S.C. Image acquisition and analyses were performed by M.B., F.Z.K. and E.G. The manual segmentations and clean-up of tissue and cellular components were performed by F.Z.K., M.B. and C.F.G. B.D.d.S. performed the mathematical and computational analyses. A.L. generated 3D images and videos. C.F.G., S.C. and E.G. supervised the work. C.F.G. obtained the financial grants. All authors actively participated in the writing of the manuscript.

Competing interests

The authors declare no competing interests.

Additional information

Supplementary information The online version contains supplementary material available at https://doi.org/10.1038/s42003-021-02919-z.

Correspondence and requests for materials should be addressed to Etienne Gontier or Christophe F. Grosset.

Peer review information *Communications Biology* thanks the anonymous reviewers for their contribution to the peer review of this work. Primary Handling Editors: Chao Zhou and Karli Montague-Cardoso.